

Convective patterns in rotating binary mixtures

Krishna Kumar

Institut für Theoretische Physik, Universität des Saarlandes, D-6600 Saarbrücken, West Germany

(Received 6 October 1989)

A few-mode Lorenz-like model for convection in a rotating binary mixture confined between stress-free, impermeable boundaries is presented. It describes for positive separation ratios standing patterns of convective rolls in mutually perpendicular directions and the superposition of these rolls with the same wave number. The model is used to investigate the effect of slow rotation on convective patterns. In ideal systems squares are unstable, and the dynamical behavior immediately in the Rayleigh regime is chaotic. Side-wall forcing is incorporated by introducing a small inhomogeneity into the model. In the presence of side walls the chaotic behavior disappears, squares are stabilized close to onset, and rolls are stable in the Rayleigh regime with oscillations occurring in between. For Taylor numbers above a critical value, oscillations disappear and stable stationary patterns are possible over the whole range of Rayleigh numbers.

I. INTRODUCTION

Convection in a horizontal layer of a binary liquid mixture¹ without rotation has been investigated extensively in recent years. The presence of concentration currents, in addition to thermal currents, leads to interesting linear and nonlinear behavior.²⁻¹⁰ The selection of different convective patterns in different regions of the Rayleigh number and the competition of these patterns in an intermediate region have been studied both experimentally⁶ and theoretically.^{9,10} The theoretical treatment⁹ based on the Galerkin technique explains effectively the phenomenon of competing patterns. Rotation, on the other hand, not only delays the onset of convection, but distorts the convective cells.^{11,12} In addition, stationary roll patterns can be destabilized by disturbances with wave vectors noncoincident with those of the patterns, giving rise to turbulent behavior^{13,14} close to the threshold.

A horizontal layer of a rotating binary liquid heated from below, naturally, represents a versatile system for the study of convective instability. Recent studies¹⁵ on these systems address the case of when convection sets in in the form of cylindrical rolls.

In this work we present a Lorenz-like model^{9,16} that describes convective patterns in the form of rolls as well as squares—the patterns arising from the superposition of mutually perpendicular rolls. Here and throughout this paper, we use the word “superposition” to describe the structure seen, e.g., in a shadowgraph picture. The fields in square convection are not just linear combinations of the roll fields. We use the model to study the influence of a small coriolis force on the competing convective patterns and their heat transport behavior.

We introduce the hydrodynamic system in Sec. II. In Sec. III we present the Galerkin model for rotating binary liquids with impermeable horizontal surfaces and discuss the results of linear stability analysis. In Sec. IV we investigate the stationary solutions describing convective patterns in the form of rolls and squares, and the

time dependent solutions arising because of competition between these patterns. We discuss the effect of side walls in Sec. V by phenomenologically introducing a constant inhomogeneity into our model. We shall see that the stationary squarelike patterns arising from superposition of mutually perpendicular rolls of unequal intensities are possible in the rotating system in the presence of side-wall forcing. We summarize the results of our model in Sec. VI.

II. HYDRODYNAMIC SYSTEM

An infinite horizontal layer of a binary liquid heated from below and rotating with a uniform angular velocity about the vertical axis is considered. Neglecting the Dufour effect, the equations of motion for the variable fields (deviations from the conductive state) in the rotating frame can be written, in the Oberbeck-Boussinesq approximation, as

$$\partial_t \mathbf{U} + (\mathbf{U} \cdot \nabla) \mathbf{U} = -\nabla(p/\rho_m) - \mathbf{g}(\alpha\Theta + \beta\mathcal{C}) + \nu \nabla^2 \mathbf{U} + 2\mathbf{U} \times \boldsymbol{\Omega}, \quad (2.1)$$

$$\partial_t \Theta + (\mathbf{U} \cdot \nabla) \Theta = \lambda \nabla^2 \Theta - (\mathbf{U} \cdot \nabla) T_s, \quad (2.2)$$

$$\partial_t \mathcal{C} + (\mathbf{U} \cdot \nabla) \mathcal{C} = D(\nabla^2 \mathcal{C} + k_T/T_m \nabla^2 \Theta) - (\mathbf{U} \cdot \nabla) C_s, \quad (2.3)$$

where $\mathbf{U}(\mathbf{x}, t)$, $p(\mathbf{x}, t)$, $\Theta(\mathbf{x}, t)$, and $\mathcal{C}(\mathbf{x}, t)$ are, respectively, velocity, pressure, temperature, and concentration fields. $\boldsymbol{\Omega} (= 0, 0, \Omega)$ is the rotation speed of the layer, \mathbf{g} the acceleration due to gravity, $\alpha(\beta)$ the thermal (solutorial) expansion coefficient at constant concentration (temperature) and pressure, ν the kinematic viscosity, $\lambda(D)$ the thermal (mass) diffusivity, and k_T the thermodiffusion coefficient. T_s and C_s stand for the temperature and concentration profiles in the conductive state and can be written for small temperature difference ΔT across the layer of thickness d as

$$T_s = T_l - (\Delta T/d)x_3, \quad (2.4)$$

$$C_s = C_1 + (k_T/T_m)(\Delta T/d)x_3, \quad (2.5)$$

where T_1 and C_1 are the temperature and the concentration at the bottom layer. Here we ignored the centrifugal force acting on temperature and concentration induced density variations.

Introducing dimensionless variables $\theta = \Theta \alpha g d^3 / \nu \lambda$ and $C = \mathcal{C} \beta g d^3 / \nu \lambda$, and scaling all the lengths by d , the thickness of the layer, and time by d^2 / λ , the thermal diffusion time across the layer, we can put the hydrodynamic equations in nondimensional form as

$$\partial_t \nabla^2 u_3 = \sigma \nabla^4 u_3 + \sigma \nabla_1^2 [(1 + \psi)\theta + \eta] - \sigma \sqrt{\mathcal{T}} \partial_3 \omega_3 - \hat{\mathbf{e}}_3 \cdot \nabla \times [(\boldsymbol{\omega} \cdot \nabla) \mathbf{u} - (\mathbf{u} \cdot \nabla) \boldsymbol{\omega}], \quad (2.6)$$

$$\partial_t \omega_3 = \sigma \nabla^2 \omega_3 + \sigma \sqrt{\mathcal{T}} \partial_3 u_3 + [(\boldsymbol{\omega} \cdot \nabla) u_3 - (\mathbf{u} \cdot \nabla) \omega_3], \quad (2.7)$$

$$\partial_t \theta = \nabla^2 \theta + R u_3 - (\mathbf{u} \cdot \nabla) \theta, \quad (2.8)$$

$$\partial_t \eta = L \nabla^2 \eta - \psi \nabla^2 \theta - (\mathbf{u} \cdot \nabla) \eta, \quad (2.9)$$

where the mixed field

$$\eta = C - \psi \theta \quad (2.10)$$

is used to enforce the impermeability of the mass current at the two horizontal surfaces of the layer in a convenient way. $\boldsymbol{\omega} = \nabla \times \mathbf{u}$ is the vorticity, $\sigma (= \nu / \lambda)$ the Prandtl number, $L (= D / \lambda)$ the Lewis number, $R [= \alpha g (\Delta T) d^3 / \nu \lambda]$ the Rayleigh number, $\mathcal{T} (= 4 \Omega^2 d^4 / \nu^2)$ the Taylor number, and ψ the separation ratio. The subscripts 1 and 2 refer to two mutually perpendicular directions in horizontal plane, while 3 refers to vertically upward direction. $\hat{\mathbf{e}}_3$ is a unit vector along the x_3 axis.

Since the influence of the “no-slip” properties of the horizontal boundaries on thermal convection in liquids seems to be less important,^{9,17} we consider stress-free surfaces. This implies $u_3 = \partial_3^2 u_3 = \partial_3 \omega_3 = 0$ at $x_3 = 0$ and 1. We impose impermeability to capture the essential physics due to additional coupling between the temperature and the concentration gradients at the horizontal boundaries. The temperature fluctuation $\theta = 0$ at $x_3 = 0$ and 1, which corresponds to perfectly conducting surfaces.

III. GALERKIN MODEL

A. Selection of modes

We employ the standard Galerkin procedure to describe convection in a rotating binary mixture. The spatial dependence of all the fields are expanded in a Fourier series appropriate to the horizontal free-slip, impermeable boundaries, and lateral periodic boundary conditions. The expansion is truncated to describe straight

rolls and patterns arising from the superposition of mutually perpendicular rolls of the same wavelength. Here, we restrict ourselves to standing patterns and, hence all time-dependent Fourier amplitudes will be assumed to be real.

The rotation couples the vertical components of velocity and vorticity [Eqs. (2.6) and (2.7)], the coupling being $\sigma \sqrt{\mathcal{T}}$. Thus we have one additional basic mode for the latter besides other critical modes which can grow at the onset of convection according to the linearized system of hydrodynamic equations [Eqs. (2.6)–(2.9)]. We retain those higher modes, which are coupled to the critical modes through the convective interaction and are compatible with the boundary conditions on the hydrodynamic fields. Modes representing higher lateral harmonic variations of the fields are neglected.

With above consideration the vertical component of the velocity field reads as

$$u_3(\mathbf{x}, t) = [a_1(t) \cos(kx_1) + a_2(t) \cos(kx_2)] \sin(\pi x_3) + 2[a_3(t) \cos(kx_1) \cos(kx_2) + \bar{a}_3(t) \sin(kx_1) \sin(kx_2)] \sin(2\pi x_3). \quad (3.1)$$

The vertical component of the vorticity is given by

$$\omega_3(\mathbf{x}, t) = [b_1(t) \cos(kx_1) + b_2(t) \cos(kx_2)] \cos(\pi x_3) + 2[b_3(t) \cos(kx_1) \cos(kx_2) + \bar{b}_3(t) \sin(kx_1) \sin(kx_2)] \cos(2\pi x_3). \quad (3.2)$$

The temperature field can be written as

$$\theta(\mathbf{x}, t) = [c_1(t) \cos(kx_1) + c_2(t) \cos(kx_2)] \sin(\pi x_3) + 2[c_3(t) \cos(kx_1) \cos(kx_2) + \bar{c}_3(t) \sin(kx_1) \sin(kx_2)] \sin(2\pi x_3) + c_4(t) \sin(2\pi x_3), \quad (3.3)$$

and the mixed field

$$\eta(\mathbf{x}, t) = d_1(t) \cos(kx_1) + d_2(t) \cos(kx_2) + [d_3(t) + \bar{d}_3(t) \sin(kx_1) \sin(kx_2)] \cos(\pi x_3). \quad (3.4)$$

The equation of continuity and the solenoidal character of the vorticity yield the following expressions for horizontal components of velocity and vorticity fields:

$$u_1(\mathbf{x}, t) = -\frac{1}{k} ([\pi a_1(t) \sin(kx_1) + b_2(t) \sin(kx_2)] \cos(\pi x_3) + \{[2\pi a_3(t) - \bar{b}_3(t)] \sin(kx_1) \cos(kx_2) - [2\pi \bar{a}_3(t) - b_3(t)] \cos(kx_1) \sin(kx_2)\} \cos(2\pi x_3)), \quad (3.5)$$

$$u_2(\mathbf{x}, t) = -\frac{1}{k} ([\pi a_2(t) \sin(kx_2) - b_1(t) \sin(kx_1)] \cos(\pi x_3) + \{[2\pi a_3(t) + \bar{b}_3(t)] \cos(kx_1) \sin(kx_2) - [2\pi \bar{a}_3(t) + b_3(t)] \sin(kx_1) \cos(kx_2)\} \cos(2\pi x_3)), \quad (3.6)$$

$$\omega_1(\mathbf{x}, t) = -\frac{1}{k} ((\pi^2 + k^2) a_2(t) \sin(kx_2) - \pi b_1(t) \sin(kx_1)) \sin(\pi x_3) + 2\{[(2\pi^2 + k^2) a_3(t) + \pi \bar{b}_3(t)] \cos(kx_1) \sin(kx_2) - [(2\pi^2 + k^2) \bar{a}_3(t) + \pi b_3(t)] \sin(kx_1) \cos(kx_2)\} \sin(2\pi x_3), \quad (3.7)$$

$$\begin{aligned} \omega_2(\mathbf{x}, t) = & \frac{1}{k} \{[(\pi^2 + k^2)a_1(t)\sin(kx_1) + \pi b_2(t)\sin(kx_2)]\sin(\pi x_3) \\ & + 2\{[(2\pi^2 + k^2)a_3(t) - \pi\bar{b}_3(t)]\sin(kx_1)\cos(kx_2) \\ & - [(2\pi^2 + k^2)\bar{a}_3(t) - \pi b_3(t)]\cos(kx_1)\sin(kx_2)\}\sin(2\pi x_3)\}. \end{aligned} \quad (3.8)$$

The fact that rotation distorts convective patterns¹² is taken care of by the form of the velocity field [Eqs. (3.1), (3.5), and (3.6)]. For the case of roll patterns, stream lines are elliptical instead of being circular, and the normal, $\mathbf{n} = n_1\hat{e}_1 + n_2\hat{e}_2$, to the plane of stream lines forms an angle with the roll axis. This is because of the growth of the other component of velocity (e.g., u_2 , which is not present in the absence of rotation if rolls are along the x_2 axis) under the action of coriolis force. Consequently, the mirror symmetry of the pattern about a vertical plane through the maximal up (down) flow locations is lost. A translation by half a wavelength in a direction normal to the rolls leads to similar patterns with reversed flow directions. To describe a general square pattern arising from the superposition of mutually perpendicular set of these rolls, it is essential to include the nonlinear mode \bar{a}_3 in addition to a_3 , in the expansion for vertical component of the velocity field. This leads to other nonlinear modes \bar{b}_3 , \bar{c}_3 , and \bar{d}_3 in our model.

B. Model equations

Projecting the hydrodynamic equations [Eqs. (2.6)–(2.10)] onto the above-mentioned modes, and properly rescaling the variables, we arrive at the following Lorenz-like¹⁶ model:

$$\begin{aligned} \gamma\dot{\mathbf{X}} = & -\sigma\hat{q}^2\mathbf{X} + \sigma\frac{\hat{k}^2}{\hat{q}^2}\left[(1+\psi)\mathbf{Y} + \frac{8}{\pi^2}\mathbf{U}\right] - \frac{\sigma}{\hat{q}^2}\sqrt{\tau}\mathbf{G} \\ & + \begin{bmatrix} X_2 \\ X_1 \end{bmatrix} S_1 - \frac{1}{\hat{q}^2} \begin{bmatrix} G_2 \\ G_1 \end{bmatrix} \mathbf{W}_1 + \begin{bmatrix} G_2 \\ -G_1 \end{bmatrix} S_2 \\ & - \frac{\hat{d}_2^2}{2\hat{q}^2} \begin{bmatrix} X_2 \\ -X_1 \end{bmatrix} \mathbf{W}_2, \end{aligned} \quad (3.9)$$

$$\begin{aligned} \gamma\dot{\mathbf{Y}} = & -\hat{q}^2\mathbf{Y} + (r - Z)\mathbf{X} + \begin{bmatrix} X_2 \\ X_1 \end{bmatrix} T_1 \\ & + \begin{bmatrix} G_2 \\ -G_1 \end{bmatrix} T_2 + \frac{1}{2} \begin{bmatrix} Y_2 \\ -Y_1 \end{bmatrix} \mathbf{W}_2, \end{aligned} \quad (3.10)$$

$$\gamma\dot{\mathbf{U}} = -\hat{k}^2 b' L \mathbf{U} + \psi \hat{q}^2 \mathbf{Y} + \mathbf{X} V_1 + \begin{bmatrix} G_2 \\ -G_1 \end{bmatrix} V_2, \quad (3.11)$$

$$\begin{aligned} \gamma\dot{\mathbf{G}} = & -\sigma\hat{q}^2\mathbf{G} + \sigma\sqrt{\tau}\mathbf{X} + \begin{bmatrix} X_2 \\ X_1 \end{bmatrix} \mathbf{W}_1 + \begin{bmatrix} G_2 \\ G_1 \end{bmatrix} S_1 \\ & + \frac{b}{4} \begin{bmatrix} X_2 \\ -X_1 \end{bmatrix} S_2 + \frac{1}{2} \begin{bmatrix} G_2 \\ -G_1 \end{bmatrix} \mathbf{W}_2, \end{aligned} \quad (3.12)$$

$$\gamma\dot{Z} = -b(Z - \mathbf{X} \cdot \mathbf{Y}), \quad (3.13)$$

$$\gamma\dot{V}_1 = -b \left[\frac{L}{4} V_1 + \frac{2}{3} \psi Z + \frac{1}{2} (\mathbf{X} \cdot \mathbf{U}) + \frac{1}{4} S_2 V_2 \right], \quad (3.14)$$

$$\begin{aligned} \gamma\dot{V}_2 = & -L\hat{d}_3^2 V_2 + \frac{8}{3} \psi \hat{d}_1^2 T_2 \\ & - 2(G_2 U_1 - G_1 U_2) + V_1 S_2, \end{aligned} \quad (3.15)$$

$$\begin{aligned} \gamma\dot{\mathbf{S}} = & -2\sigma\hat{d}_1^2 \mathbf{S} + \sigma(1+\psi)\frac{\hat{k}^2}{\hat{d}_1^2} \mathbf{T} - \frac{\sigma\sqrt{\tau}}{\hat{d}_1^2} \mathbf{W} \\ & + \frac{16\sigma}{3\pi^2} \frac{\hat{k}^2}{\hat{d}_1^2} \begin{bmatrix} 0 \\ V_2 \end{bmatrix} - \begin{bmatrix} \frac{b}{2\hat{d}_1^2} (\hat{q}^2 X_1 X_2 + G_1 G_2) \\ \frac{\hat{k}^2}{\hat{d}_1^2} b' (G_2 X_1 - G_1 X_2) \end{bmatrix}, \end{aligned} \quad (3.16)$$

$$\gamma\dot{\mathbf{T}} = -2\hat{d}_1^2 \mathbf{T} + r\mathbf{S} - \begin{bmatrix} (b/4)(X_1 Y_2 + X_2 Y_1) \\ (G_2 Y_1 - G_1 Y_2) \end{bmatrix}, \quad (3.17)$$

$$\gamma\dot{\mathbf{W}} = -2\sigma\hat{d}_1^2 \mathbf{W} + 2\sigma\sqrt{\tau}\mathbf{S}. \quad (3.18)$$

The critical modes of the above dynamical system are defined by

$$\mathbf{X} = \begin{bmatrix} X_1 \\ X_2 \end{bmatrix} = \frac{1}{2\sqrt{2}q_c} \begin{bmatrix} a_1 \\ a_2 \end{bmatrix}, \quad (3.19a)$$

$$\mathbf{Y} = \begin{bmatrix} Y_1 \\ Y_2 \end{bmatrix} = \frac{k_c^2}{2\sqrt{2}q_c^5} \begin{bmatrix} c_1 \\ c_2 \end{bmatrix}, \quad (3.19b)$$

$$\mathbf{U} = \begin{bmatrix} U_1 \\ U_2 \end{bmatrix} = \frac{\pi k_c^2}{4\sqrt{2}q_c^5} \begin{bmatrix} d_1 \\ d_2 \end{bmatrix}, \quad (3.19c)$$

$$\mathbf{G} = \begin{bmatrix} G_1 \\ G_2 \end{bmatrix} = \frac{1}{2\sqrt{2}q_c^2} \begin{bmatrix} b_1 \\ b_2 \end{bmatrix}. \quad (3.19d)$$

The modes representing heat and mass currents are

$$\mathbf{Z} = -\frac{\pi k_c^2}{q_c^6} c_4, \quad V_1 = \frac{\pi^2 k_c^2}{4q_c^6} d_3. \quad (3.19e)$$

The nonlinear modes essential to describe cylindrical rolls and superposition of mutually perpendicular rolls in rotating fluids are

$$\mathbf{S} = \begin{bmatrix} S_1 \\ S_2 \end{bmatrix} = \frac{1}{2q_c} \begin{bmatrix} \frac{\pi}{q_c} a_3 \\ \bar{a}_3 \end{bmatrix}, \quad (3.19f)$$

$$\mathbf{T} = \begin{bmatrix} T_1 \\ T_2 \end{bmatrix} = \frac{k_c^2}{2q_c^5} \begin{bmatrix} \frac{\pi}{q_c} c_3 \\ \bar{c}_3 \end{bmatrix}, \quad (3.19g)$$

$$\mathbf{W} = \begin{pmatrix} W_1 \\ W_2 \end{pmatrix} = \frac{1}{2q_c^2} \begin{pmatrix} \frac{\pi}{q_c} & b_3 \\ & \tilde{b}_3 \end{pmatrix}, \quad (3.19h)$$

$$V_2 = \frac{\pi k_c^{02}}{8q_c^5} \tilde{d}_3. \quad (3.19i)$$

In the above, we used

$$b = \frac{4\pi^2}{q_c^2}, \quad b' = \frac{k_c^{02}}{q_c^2}, \quad r = \frac{1}{q_c^2}. \quad (3.20)$$

The reduced quantities are defined as

$$\hat{q}^2 = \frac{\pi^2 + k^2}{q_c^2}, \quad \hat{k}^2 = \frac{k^2}{k_c^{02}}, \quad \hat{d}_1^2 = \frac{2\pi^2 + k^2}{q_c^2},$$

$$\hat{d}_2^2 = \frac{\pi^2 - k^2}{q_c^2}, \quad \hat{d}_3^2 = \frac{\pi^2 + 2k^2}{q_c^2}, \quad (3.20b)$$

$$r = \frac{Rk_c^{02}}{q_c^6}, \quad \tau = \frac{\pi^2 \mathcal{T}}{q_c^6},$$

with

$$q_c^2 = \pi^2 + k_c^{02}. \quad (3.20c)$$

Here k_c^0 is the critical wave number for a one-component rotating fluid, and is given by

$$k_c^0 = k_c(\psi=0, \mathcal{T}) = \pi(l_1 + l_2 - \frac{1}{2})^{1/2}, \quad (3.20d)$$

with

$$l_{1,2} = \left[\frac{1}{4} \left\{ \frac{1}{2} + \frac{\mathcal{T}}{\pi^4} \pm \left[\left(\frac{1}{2} + \frac{\mathcal{T}}{\pi^4} \right)^2 - \frac{1}{4} \right]^{1/2} \right\} \right]^{1/3}. \quad (3.20e)$$

In the absence of rotation $k_c(\psi=0, \mathcal{T}=0) = \pi/\sqrt{2}$, the critical wave number for a one-component fluid with free-slip surfaces.

C. Linear stability analysis

The critical convective modes \mathbf{X} , \mathbf{Y} , \mathbf{U} , and \mathbf{G} start growing according to the linearized equations of the model as the conductive steady state ($\mathbf{X}=\mathbf{Y}=\mathbf{U}=\mathbf{G}=0$) is destabilized. The threshold for stationary instability is found to be

$$r_s(\psi, k, \tau) = \frac{(\hat{q}^6 + \tau)}{\hat{k}^2} \left[1 + \psi + \frac{8}{\pi^2} \frac{\psi}{b'L} \frac{\hat{q}^2}{\hat{k}^2} \right]^{-1}, \quad (3.21)$$

which means

$$R_s(\psi, k, \mathcal{T}) = \left[\frac{(\pi^2 + k^2)^3 + \pi^2 \mathcal{T}}{(1 + \psi)k^2 + (8/\pi^2)(\psi/L)(\pi^2 + k^2)} \right]. \quad (3.22)$$

The critical wave number is obtained from $\partial^2 R_s / \partial k^2 = 0$. For positive ψ (we restrict ourselves to $\psi > 0$ throughout this paper), this yields

$$3[\pi^2 + k_c^2(\psi, \mathcal{T})]^2 \left[\left[1 + \psi + \frac{8}{\pi^2} \frac{\psi}{L} \right] k_c^2(\psi, \mathcal{T}) + \frac{8\psi}{L} \right] = \{[\pi^2 + k_c^2(\psi, \mathcal{T})]^3 + \pi^2 \mathcal{T}\} \left[1 + \psi + \frac{8}{\pi^2} \frac{\psi}{L} \right]. \quad (3.23)$$

The condition for vanishing critical wave number [$k_c(\psi, \mathcal{T})=0$] comes out to be

$$\psi_0 \approx L(1 + \mathcal{T}/\pi^4) / \left[\frac{16}{\pi^2} - L - \frac{\mathcal{T}L}{\pi^4} \left[1 + \frac{8}{\pi^2} \right] \right]. \quad (3.24)$$

The expression (3.24) shows clearly that above a certain Taylor number

$$\mathcal{T}_0 \geq \frac{(16/L - \pi^2)\pi^2}{(1 + 8/\pi^2)}, \quad (3.25)$$

the possibility of a vanishing critical wave number does not exist.

The wave number $k(\psi, \mathcal{T})$ is a function of both ψ and \mathcal{T} . We have used $k_c(\psi=0, \mathcal{T})$ as the reference critical wave number. On the other hand, in absence of rotation, experiments⁶ show that the wavelength of the fully developed convective patterns is almost the same as in the case of pure (one-component) fluid over a wide range of ψ . Hence, hereafter, we set $\hat{k} = k/k_c(\psi=0, \mathcal{T}) = 1$.

IV. CONVECTIVE PATTERNS IN IDEAL SYSTEM

Here we discuss different convective patterns possible within our model in the absence of any imperfection and their stability behavior. In Sec. V, we shall see that even small inhomogeneities simulating side-wall forcing can lead to important changes.

A. Stationary convection

The fixed points corresponding to different stationary convective patterns are the nontrivial solutions of the model with time derivatives set equal to zero. There is a set of two mutually perpendicular cylindrical rolls. Similar rolls with reversed flow directions are also possible. Thus there are four equivalent fixed points corresponding to roll patterns. The superposition of these rolls gives rise to square pattern, which we shall discuss shortly.

1. Rolls

To be specific let us consider the set of rolls parallel to the x_2 axis, i.e.,

$$X_2 = Y_2 = U_2 = G_2 = 0. \quad (4.1)$$

Consequently, all the nonlinear modes, except \mathbf{Z} and V_1 , representing heat and mass transport, respectively, decouple from the system of Eqs. (3.9)–(3.18). The roll state is given by

$$\begin{aligned}
Y_1 &= \frac{rX_1}{(1+X_1^2)}, \\
U_1 &= \frac{r\psi}{b'}(L/6 - \frac{4}{9}X_1^2) \frac{X_1}{(1+X_1^2)} \frac{1}{(L^2/6+X_1^2)}, \\
G_1 &= \sqrt{\tau}X_1, \quad Z = \frac{rX_1^2}{(1+X_1^2)}, \\
V_1 &= -\frac{r\psi(1+\frac{4}{9}L)}{(L^2/6+X_1^2)} \frac{X_1^2}{(1+X_1^2)},
\end{aligned} \tag{4.2a}$$

with X_1^2 being the positive root of

$$X_1^4 + AX_1^2 + B = 0, \tag{4.2b}$$

where

$$A = 1 + L^2/6 - \frac{r}{r_s(\tau)} \frac{(1 + \psi - 32\psi/9b'\pi^2)}{(1 + \psi + 8\psi/\pi^2b'L)} \tag{4.2c}$$

and

$$B = -L^2/6[r/r_s(\tau) - 1]. \tag{4.2d}$$

X_1 , and hence the Nusselt number, depends on τ through $b'[=k_c^{02}(\tau)/q_c^2(\tau) = \frac{1}{3}(1+\tau)]$ even for fixed values of $r/r_s(\tau)$.

2. Squares

Under the action of a coriolis force the square cell is distorted and the streamlines, as in the case of the roll pattern, lose mirror symmetry. However, the positions of maximal up and down flows still remain on the four vertices of a square. A translation in x_1 and x_2 directions by half a wavelength results in a similar pattern with reversed flow directions. Nonlinear modes \mathbf{S} , \mathbf{T} , \mathbf{W} , and V_2 arise because of convective nonlinearity (e.g., $\mathbf{u} \cdot \nabla \theta$). In the absence of these modes, rolls (in the x_1 and x_2 directions) cannot be distinguished from square patterns. Depending upon the convective field intensity, the superposition of mutually perpendicular rolls can give rise to two kinds of patterns.

Case I. Superposition of rolls of equal intensities (S patterns). In this case we have

$$|X_1| = |X_2| \neq 0. \tag{4.3}$$

The corresponding patterns will be referred to as square S patterns. Note that the nonlinear modes V_2 , S_2 , and T_2 [Eqs. (3.15)–(3.17)] are excited by the nonlinear interaction of critical modes only through the combinations $(G_2U_1 - G_1U_2)$, $(G_2X_1 - G_1X_2)$, and $(G_2Y_1 - G_1Y_2)$, respectively. In the present case, these combinations always vanish and therefore V_2 , S_2 , T_2 , and consequently W_2 decouple from the system. We need only 13 modes to describe the S patterns. First we investigate this kind of pattern in the limit of large Prandtl number ($\sigma \gg 1$). In this case two more nonlinear modes (S_1 and W_1) drop out, and the fixed points of the eleven-mode model read

$$X_2^2 = X_1^2, \quad \mathbf{Y} = \frac{r\mathbf{X}}{[1 + 2X_1^2(1 + b/8\hat{d}_1^2)]}, \tag{4.4a}$$

$$\mathbf{U} = \frac{\psi(L - \frac{16}{3}X_1^2)}{(b'L^2 + 4X_1^2)} \mathbf{Y}, \quad \mathbf{G} = \sqrt{\tau}\mathbf{X},$$

$$\mathbf{Z} = \mathbf{X} \cdot \mathbf{Y}, \quad V_1 = -\frac{2}{L}(\frac{4}{3}\psi\mathbf{Y} + \mathbf{U}) \cdot \mathbf{X}, \tag{4.4b}$$

$$T_1 = -\text{sgn}(X_1X_2) \frac{b}{8\hat{d}_1^2} (\mathbf{X} \cdot \mathbf{Y}),$$

with X_1^2 is the positive root of

$$X_1^4 + \tilde{A}X_1^2 + \tilde{B} = 0, \tag{4.5}$$

where

$$\begin{aligned}
\tilde{A} &= \frac{1}{2[1 + (b/8)\hat{d}_1^2]} \\
&\times \left[1 + \frac{b'L^2}{2} \left[1 + \frac{b}{8\hat{d}_1^2} \right] \right. \\
&\quad \left. - \frac{(1 + \psi - 32\psi/3\pi^2)}{[1 + \psi + (8/\pi^2)(\psi/b'L)]} \frac{r}{r_s(\tau)} \right]
\end{aligned} \tag{4.6a}$$

and

$$\tilde{B} = -\frac{b'L^2}{8(1 + b/8\hat{d}_1^2)} \left[\frac{r}{r_s(\tau)} - 1 \right]. \tag{4.6b}$$

For $r > r_s(\tau)$, \tilde{B} is always negative and hence the positive root of Eq. (4.5) exists.

In the case of a finite Prandtl number fluid, we find the fixed points numerically using a Newton algorithm. The pattern exists and the dependence of fixed points on τ is slightly stronger.

Case II. Superposition of rolls of unequal intensities (S' patterns). Here, we have

$$|X_1| \neq |X_2| \neq 0. \tag{4.3'}$$

In this situation, the nonlinear modes S_2 , T_2 , V_2 , and W_2 cannot be dropped out. And, consequently, the superposed rolls will give rise to a square pattern similar to the previous case, but with checkerboardlike structure. The intensity of the fields will be relatively higher in the two neighboring quadrants along a diagonal compared to that in other two quadrants. We shall refer to these patterns as squarelike S' patterns. When $|X_1|$ or $|X_2|$ goes to zero, we have a roll pattern. We have not found stable S' patterns numerically in the ideal system. However, in presence of any imperfection this state may be possible (cf. Sec. V).

3. Nusselt number

The Nusselt number—the ratio of laterally averaged heat current at the lower layer and conductive heat current—is given in terms of our model variable as

$$\mathcal{N} = \frac{2Z}{r} + 1. \tag{4.7}$$

Figure 1(a) presents a plot of the Nusselt number as a function of the reduced Rayleigh number for stationary roll patterns at different Taylor numbers. With increasing Taylor number, the threshold for convection increases [Eq. (3.21)] and consequently, the Soret regime (with small slope) as well as the Rayleigh regime (with large slope ≈ 2 for $\mathcal{T}=0$) are shifted towards higher r . The slope of the curve decreases slowly with increasing \mathcal{T} .

In Fig. 1(b), we show the same plot for stationary square S pattern. As in the previous case, the curve is shifted to higher r values but the slope of the curve decreases faster than in case of rolls.

4. Stability

We carry out the stability analysis for the stationary patterns numerically by evaluating the eigenvalues of the 17×17 matrix obtained by linearizing the model around the corresponding fixed points. The square S patterns are found to be unstable. The positive eigenvalues are very small in the Soret regime and sufficiently large in the Rayleigh regime. On the other hand, roll patterns are

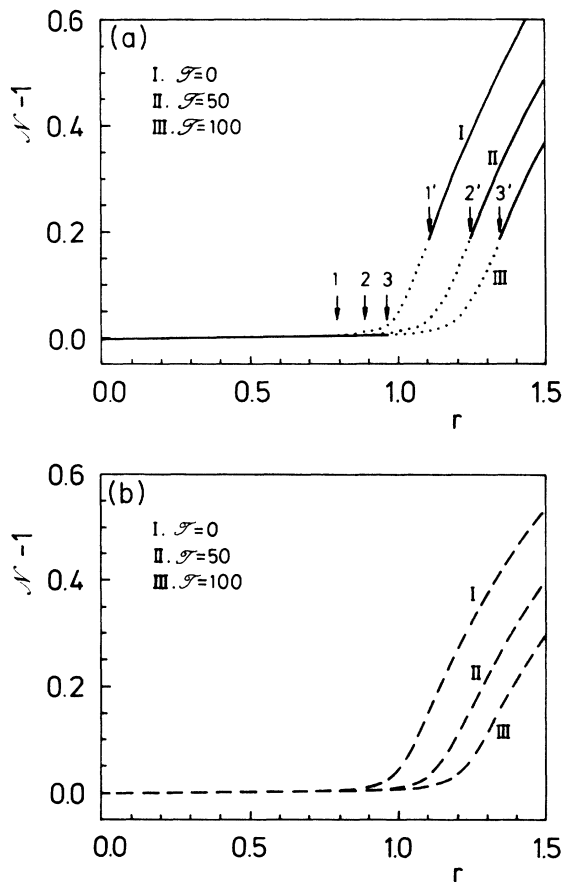


FIG. 1. The Nusselt number vs the reduced Rayleigh number at different Taylor numbers for stationary (a) roll and (b) square patterns. Dots indicate unstable rolls. The window of unstable rolls are marked by arrows labeled nn' ($n=1,2,3$). Squares are always unstable, although weakly unstable in the Soret regime. The threshold for the onset of convection is not marked in the figures. Parameters are $\sigma=23$, $\psi=0.1$, and $L=0.018$.

quite stable in the far Rayleigh regime. In the Soret regime the negative eigenvalues are very small. Roll patterns are, however, unstable in a small window of Rayleigh numbers [shown in Fig. 1(a) by dotted lines] in the transition region between two convective regimes. The stability behavior of the stationary patterns remain somehow similar to the case of no rotation. However, the dynamical behavior in the Rayleigh regime (cf. Sec. IV B) is interesting.

B. Time-dependent convection

We study time-dependent solutions by numerically integrating our full model. We investigate the dynamic character of the patterns in two ways—first by finding the time-dependent solutions with $\mathcal{T}=0$ and then studying their development with increasing \mathcal{T} ; and second by studying solutions for fixed \mathcal{T} with increasing r . Both yield, with suitable initial conditions, the same behavior.

In the absence of rotation, Müller and Lücke⁹ found oscillatory patterns around $r=1$. In the Soret regime, they observed either ellipselike orbits centered around the origin or straight lines through the origin in the X_1 - X_2 plane (or the plane of shadowgraphy). In the Rayleigh regime they found circular-shaped orbits. We do see these behaviors. In the Soret regime, however, we find that these trajectories always lie on one of the axes in the X_1 - X_2 plane. The trajectories oscillate at one side of the origin before crossing over to the other side of the origin, and the amplitude of oscillations changes randomly with time. Thus the sequence of appearance, disappearance, and reappearance of roll patterns with globally reversed flow directions seems to be random. Only for $r=1$ is there a simple periodic sequence.

In the presence of rotation ($\mathcal{T} \neq 0$) the time-dependent behavior becomes more complex. In the Soret regime,

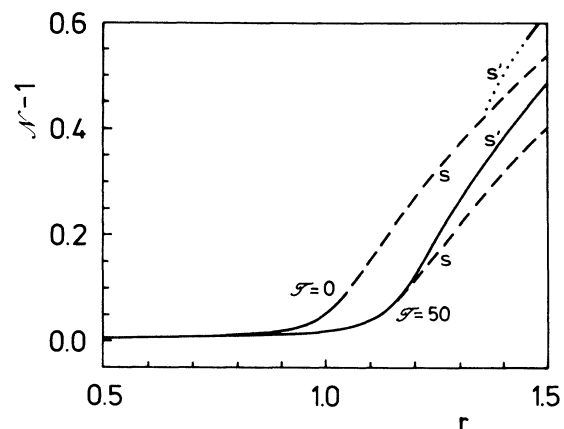


FIG. 2. The Nusselt number vs the reduced Rayleigh number at different Taylor numbers for stationary patterns (in the presence of inhomogeneity). Solid line indicates stable stationary patterns. The upper branch of both the curves corresponds to S' and at higher r to roll patterns, while the lower branch corresponds to S patterns. The dots and dashed line represent, respectively, unstable S' and S patterns. At lower r , there exists only one branch representing S patterns. Inhomogeneity, $\xi_i=0.005$, and other parameters are as in Fig. 1.

the size of straight-line-like orbits on the X_1 (or X_2) axis grows, and, in addition, the time variation of the trajectories becomes more complicated. Now the trajectories remain on one side of the origin for a longer time, wandering randomly around the stationary roll fixed point and the origin, and then cross over to the other side of the origin.

On the other hand, the effect of rotation is more interesting in the Rayleigh regime. At smaller Taylor numbers (\mathcal{T}), the circular shaped orbits are distorted. With increasing \mathcal{T} , the shape changes to distorted squarelike orbits. At higher \mathcal{T} the limit cycle breaks, and the trajectory wanders chaotically in the phase space. This corresponds to a chaotic sequence of an alternating sequence of roll and square patterns. If \mathcal{T} is enhanced further, the basin of these chaotic trajectories expands. At relatively higher \mathcal{T} , the projection of the phase space on the X_1 - X_2 plane look like straight lines lying on the axes—typical of the behavior in the Soret regime. This is so because at these values of \mathcal{T} , the shift in Nusselt number is enough to drag the system into the Soret regime.

Here we mention, as an aside, that the modes V_2 , S_2 , T_2 , and W_2 are smaller compared to other modes, but nevertheless, finite. In the Rayleigh regime they cannot be ignored in comparison to other nonlinear modes. Thus they can, in the presence of any inhomogeneity in the system, give rise to important changes (Sec. V) in the stationary as well as the dynamical behavior of the system.

V. CONVECTIVE PATTERNS IN REALISTIC SYSTEM

In experimental cells, there are side walls that favor a particular pattern. This is so because the local flow directions near the walls are fixed, and consequently the degeneracy of convective patterns is lifted. However, there is no exact way to study side-wall effects theoretically, even in the absence of rotation. Ahlers, Hohenberg, and Lücke¹⁸ incorporated the side-wall forces caused by temperature modulation by introducing inhomogeneous terms into their Galerkin model. Recently, Müller and Lücke⁹ added a constant inhomogeneity to the equation for mixed field in their Lorenz-like model for binary mixture and found good agreement with the experiments of Moses and Steinberg.⁶

We do not think the mechanism of side-wall forcing is totally different in the rotating frame of reference. Therefore we try to incorporate the effect with a constant inhomogeneity ξ in the equation for mixed field. In what follows we present the results of our model with Eq. (3.11) replaced by

$$\dot{\mathbf{U}} = -b'LU + \psi\mathbf{Y} + \mathbf{X}V_1 + \begin{bmatrix} G_2 \\ -G_1 \end{bmatrix} V_2 + \xi. \quad (5.1)$$

\hat{k} and \hat{q} are set equal to unity as in the preceding sections. We choose $\xi_1 = \xi_2$, which corresponds to forcing caused by a square cell.

A. Stationary convection

We determine the fixed points corresponding to a stationary pattern in the presence of a small inhomogeneity

($\xi_1 = \xi_2 > 0$) in the system numerically by a Newtonian algorithm. The stability of stationary patterns is investigated by evaluating the eigenvalues of the associated 17×17 matrix as described in Sec. IV.

In the absence of rotation, as reported by Müller and Lücke,⁹ we observe stable square S patterns in the Soret regime, while stable roll patterns are seen in the Rayleigh regime well above $r=1$. Here, the roll solution means the convective amplitude of one set of rolls is much larger than that of the other set normal to the former. As the Rayleigh number is lowered, the convective amplitudes of the latter set of rolls grow. The patterns with X_1 comparable to X_2 are unstable.

The results of our model in the presence of inhomogeneity show, as in case of the ideal system, that the Nusselt number plot is shifted (Fig. 2) towards higher r , and the slope of the curve decreases with increasing Taylor numbers. In addition, there is an interesting feature—the window, where stationary patterns are unstable, shrinks as the Taylor number increases. The

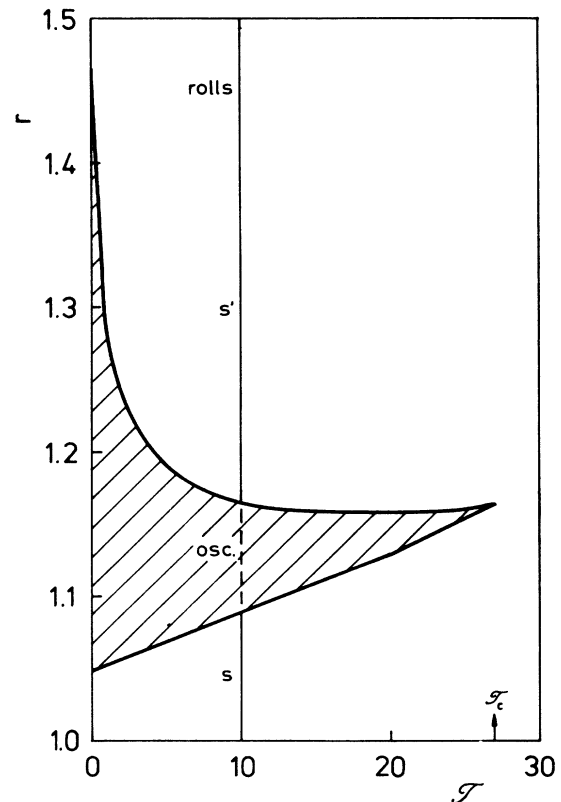


FIG. 3. Phase diagram in the r - \mathcal{T} plane. The shaded area shows the region where stationary patterns are unstable and there exist only stable oscillatory states. Marching along the vertical line (at $\mathcal{T}=10$) one finds roll patterns changing to S' patterns and the latter becoming unstable at the upper curve. However, above the upper curve stable rolls and stable oscillations coexist for some r and \mathcal{T} values. At the lower line stable square patterns appear. For $\mathcal{T} \geq \mathcal{T}_c$, there exist always-stable stationary patterns. With increasing (decreasing) Rayleigh number, there is a continuous transition from squares (rolls) to rolls (squares) through S' patterns. Parameters are $\sigma=23$, $\psi=0.1$, $L=0.018$, and $\xi_1=0.005$.

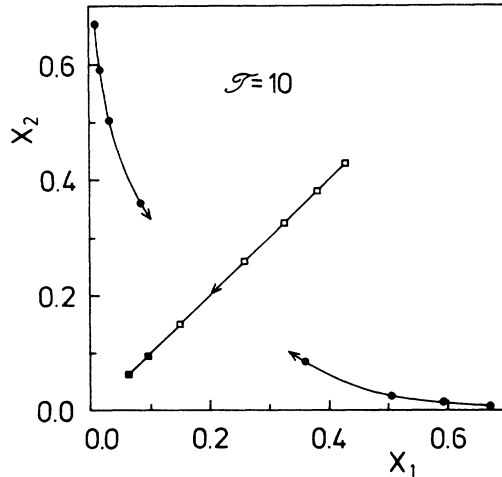


FIG. 4. Fixed points as functions of the Rayleigh number. It shows the movement of stationary fixed points in the X_1 - X_2 plane as the reduced Rayleigh number is lowered in steps of 0.1 starting at $r=1.5$ along the vertical line in Fig. 3. Open squares show unstable square patterns, while closed squares show stable square patterns. Closed circles refer to stable roll patterns changing into S' patterns as r decreases. $T=10$ and other parameters as in Fig. 3.

phase diagram in the plane of r (the reduced Rayleigh number) and T (the Taylor number) is shown in Fig. 3. Note that there exists a critical value of T ($=T_c$) above which there is always a stable stationary pattern. In the Soret regime, we always see the stable S pattern ($|X_1|=|X_2|$). In the initial Rayleigh regime the patterns become unstable for small values of T . Above T_c , however, there exists stable S' patterns in this regime. The slope of the Nusselt number is higher for this kind of pattern in comparison to the S pattern. The behavior of fixed points with the Rayleigh number is illustrated in Fig. 4. In the far Rayleigh regime, there exist two kinds of solutions—stable rolls or unstable squares (S pattern). As the Rayleigh number is lowered, the intensity of the roll pattern decays, while the intensity of the other set of

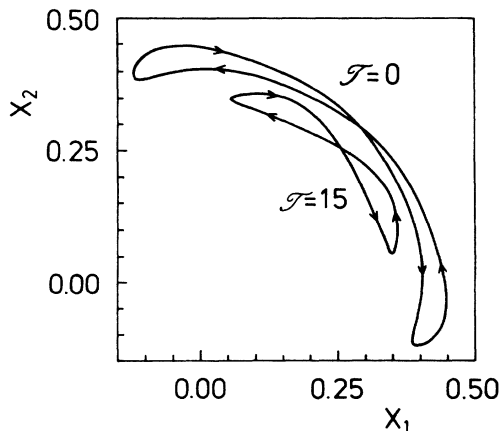


FIG. 5. Projection of limit cycle trajectories onto the X_1 - X_2 plane at different Taylor numbers ($r=1.2$). Parameters as in Fig. 3.

rolls perpendicular to the former ones start growing. Thus the fixed points corresponding to the S' pattern ($X_1 \neq X_2$) develop and move towards the line $X_1=X_2$, and in the process come nearer to the origin. On the other hand, the unstable square fixed points keep moving on the line $X_1=X_2$ towards the origin. With a further decrease of the Rayleigh number, fixed points ($|X_1| \neq |X_2|$) coming near the axes merge with the square ($|X_1|=|X_2|$) fixed points. Any further decrease in the Rayleigh number makes the only solution ($|X_1|=|X_2|$) shift towards origin. The stability of the corresponding patterns depends upon the Taylor number.

Note that the nonlinear modes V_2 , S_2 , T_2 , and W_2 of our model, which were not excited in the ideal system, are now excited in the presence of a small inhomogeneity. This leads to stable S' pattern in the initial part of the Rayleigh regime. In the Soret regime the convective amplitudes are very small and these modes are not excited. Thus we have only stable S patterns there. The threshold Rayleigh number where the solution ($|X_1| \neq |X_2|$) becomes stable depends slightly on the inhomogeneity, but the phase diagram in the plane of the Rayleigh and Taylor numbers (Fig. 3) remains qualitatively the same.

B. Time varying convection

There exists a window of the Rayleigh number, for Taylor numbers below T_c (shaded area in Fig. 3), where stationary convective patterns are always unstable.

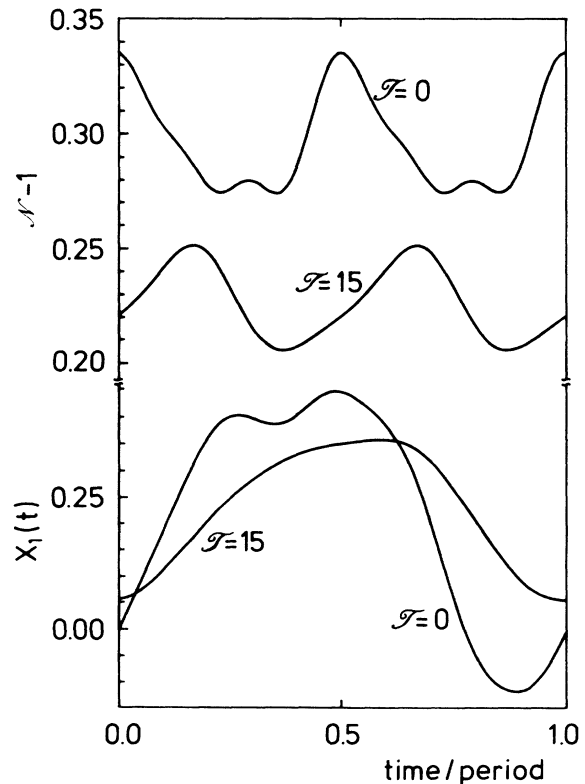


FIG. 6. The convective amplitude (X_1) and the Nusselt number for one period of the limit cycle at $r=1.2$ (Fig. 5). The amplitude and the period of oscillation decrease with increasing rotation speed, leading to a stationary pattern above a critical Taylor number.

There we find stable limit cycles. The chaotic behavior, observed in the ideal system, is suppressed. These limit cycles represent alternating S ($|X_1|=|X_2|$) and S' ($|X_1|\neq|X_2|$) patterns. Trajectories in X_1 - X_2 plane are confined almost to the first quadrant (Fig. 5). Thus the other degenerate solutions of the ideal system do not form a part of this oscillation. With increasing Taylor number, the size of the limit cycle shrinks, and depending on the Rayleigh number, S , S' , or a roll (e.g., $|X_1|\neq 0$ and $|X_2|\ll|X_1|$) pattern is obtained.

The time-dependent convective amplitude (X_1) and the Nusselt number corresponding to the limit cycles of Fig. 5 are plotted in Fig. 6. The period of the Nusselt number oscillation is always double that for the convective amplitude. The convective amplitude decreases with increasing \mathcal{T} and its time variations become more harmonic. The mean value of the Nusselt number comes down.

The oscillatory states exist even in a region (above the upper line in Fig. 3) where stationary rolls or S' patterns are stable. The size of the limit cycles decrease with increasing \mathcal{T} and oscillations disappear at $\mathcal{T}=\mathcal{T}_c$. However, there is no oscillatory state in the region of the phase space where only squares are stable (below the lower line in Fig. 3). This means, at a given Taylor number below \mathcal{T}_c , with increasing Rayleigh number the S pattern becomes unstable and the system goes to an oscillatory state through forward Hopf bifurcation, while there is hysteresis at the transition between S' patterns and the oscillatory state. For Taylor numbers above \mathcal{T}_c , there is no hysteresis.

VI. SUMMARY AND CONCLUSIONS

We have derived a quite general Lorenz model for Bénard convection in rotating binary mixtures confined between stress-free, impermeable horizontal surfaces. In the absence of rotation, our model reduces to that of Müller and Lücke.⁹ Rotation delays the onset of convection, and consequently, both the Soret as well as the Rayleigh regimes are shifted to higher Rayleigh numbers. The slope of the Nusselt number decreases with increasing rotation speed. However, the decrease in slope depends on the structure of the convective cell. For example, the decrease in the slope for the S pattern is stronger than that for the roll patterns. In the Soret regime, where the slope of the Nusselt number curve is already very small, the decrease is extremely small. On the other hand, in the Rayleigh regime the decrease is relatively higher, particularly for square S patterns.

In the ideal system, i.e., in our model without inhomogeneity, there exist two kinds of stationary patterns—a

set of degenerate rolls in mutually perpendicular directions, and patterns arising from the superposition of these rolls. Rolls are weakly stable in the Soret regime, while strongly stable in the far Rayleigh regime. However, they are unstable in a small range of Rayleigh numbers in the transition region where the Soret and the Rayleigh regimes meet together. A superposition of mutually perpendicular rolls gives rise to an S pattern ($|X_1|=|X_2|$) as well as an S' pattern ($|X_1|\neq|X_2|$). The former of these patterns is unstable in the ideal system, while the latter is not found. S patterns are weakly unstable in the Soret regime, while quite unstable in the Rayleigh regime.

In the region (for the ideal system) where there is no stable stationary patterns, there exist stable limit cycles with alternating rolls, and square patterns for very small Taylor numbers. At Taylor numbers a little higher these limit cycles break and the sequence of alternating patterns goes chaotic.

The effect of side walls is incorporated by introducing a small inhomogeneity into the model. In the presence of inhomogeneity the square S patterns are stabilized in the Soret regime, while the roll patterns remain stable in the far Rayleigh regime. The situation is similar to the case of no rotation. However, rotation makes the window of the Rayleigh number, where there are no stable stationary solutions to shrink with increasing Taylor number. This is due to the stabilization of S' patterns. At Taylor numbers below \mathcal{T}_c there exists a stable limit cycle representing alternating rolls (S' patterns) and squares. Consequently for subcritical Taylor numbers, square patterns are destabilized with increasing Rayleigh number to an oscillatory state through forward Hopf bifurcation. At Taylor numbers above \mathcal{T}_c , there exists always a stable stationary pattern.

Here we have not investigated Küppers-Lortz instability,¹³ which is likely at relatively higher Taylor numbers. In this context, it is interesting to note that in the rectangular box configuration the onset of unsteady convective flow takes place at relatively higher¹⁹ Taylor numbers, the reason being the suppression of perturbations noncoincident with convective patterns by the rectangular box, at least at small Taylor numbers.

ACKNOWLEDGMENTS

The author is indebted to Professor Dr. M. Lücke for stimulating discussions at every stage of this work and making valuable comments on the manuscript, and to the Alexander von Humboldt-Stiftung, West Germany for supporting the research. Helpful suggestions by H. W. Müller on numerical work are also acknowledged.

¹For a review see J. K. Platten and J. C. Legros, *Convection in Liquids* (Springer, Berlin, 1984).

²D. T. J. Hurle and E. Jakeman, *J. Fluid Mech.* **47**, 667 (1971).

³P. Kolodner, A. Passner, C. M. Surko, and R. W. Walden, *Phys. Rev. Lett.* **56**, 2621 (1986).

⁴E. Knobloch, *Phys. Rev. A* **34**, 1538 (1986).

⁵E. Moses and V. Steinberg, *Phys. Rev. A* **34**, 693 (1986); **35**, 1444(E) (1987).

⁶E. Moses and V. Steinberg, *Phys. Rev. Lett.* **57**, 2018 (1986).

⁷C. M. Surko and P. Kolodner, *Phys. Rev. Lett.* **58**, 2055 (1987).

⁸R. Heinrichs, G. Ahlers, and D. S. Cannell, *Phys. Rev. A* **35**, 2761 (1987).

⁹H. W. Müller and M. Lücke, *Phys. Rev. A* **38**, 2965 (1988).

¹⁰E. Knobloch, *Phys. Rev. A* **40**, 1549 (1989).

¹¹S. Chandrasekhar, *Hydrodynamic and Hydromagnetic Stability* (Oxford University Press, New York, 1961).

- ¹²For a perspective sketch of convective cells see G. Veronis, *J. Fluid Mech.* **5**, 401 (1959). See also Ref. 11.
- ¹³G. Küppers and D. Lortz, *J. Fluid Mech.* **35**, 609 (1969).
- ¹⁴J. J. Niemela and R. J. Donnelly, *Phys. Rev. Lett.* **57**, 2524 (1986).
- ¹⁵J. K. Bhattacharjee, *Phys. Fluids* **31**, 2456 (1988); **31**, 2462 (1988); **A 1**, 1938 (1989).
- ¹⁶E. N. Lorenz, *J. Atmos. Sci.* **20**, 130 (1963); see also L. N. da Costa, E. Knobloch, and N. O. Weiss, *J. Fluid Mech.* **109**, 25 (1981); J. K. Bhattacharjee and A. J. McKane, *J. Phys. A* **21**, L555 (1988).
- ¹⁷S. J. Linz and M. Lücke, *Phys. Rev. A* **35**, 3997 (1987); **36**, 2486(E) (1987).
- ¹⁸G. Ahlers, P. C. Hohenberg, and M. Lücke, *Phys. Rev. A* **32**, 3493 (1985).
- ¹⁹K. Bühler and H. Oertel, *J. Fluid Mech.* **114**, 261 (1982).